

Influence of multiphonon excitations and transfer on the fusion of Ca+Zr

H. Esbensen¹ and A. M. Stefanini²

¹*Physics Division, Argonne National Laboratory, Argonne, Illinois 60439 and*

²*INFN, Laboratori Nazionale di Legnaro, I-35020 Legnaro (Padova), Italy*

(Dated: October 1, 2018)

Abstract

Fusion data for $^{48}\text{Ca}+^{90,96}\text{Zr}$ are analyzed by coupled-channels calculations that are based on the M3Y+repulsion, double-folding potential. By applying a previously determined nuclear density of ^{48}Ca , the neutron densities of the zirconium isotopes are adjusted to optimize the fit to the fusion data, whereas the proton densities are determined by electron scattering experiments. It is shown that the fusion data can be explained fairly well by including couplings to one- and two-phonon excitations of the reacting nuclei and to one- and two-nucleon transfer reactions but there is also some sensitivity to multiphonon excitations. The neutron skin thicknesses extracted for the two zirconium isotopes are consistent with anti-proton measurements. The densities of the zirconium isotopes are used together with the previously determined nuclear density of ^{40}Ca to calculate the M3Y+repulsion potentials and predict the fusion cross sections of $^{40}\text{Ca}+^{90,96}\text{Zr}$. The predicted cross sections for $^{40}\text{Ca}+^{90}\text{Zr}$ are in reasonable agreement with the data when the influence of multiphonon excitations and a modest transfer is considered. The prediction of the $^{40}\text{Ca}+^{96}\text{Zr}$ fusion cross section, on the other hand, is poor and under-predicts the data by 30 to 40%. Although couplings to transfer channels with positive Q values were expected to play an important role, they are not able to explain the data, primarily because the predicted Coulomb barrier is about 1.5 MeV too high. Possible reasons for this failure are discussed.

PACS numbers: 21.30.Fe, 24.10.Eq, 25.60.Pj, 25.70.Jj

I. INTRODUCTION

Heavy-ion fusion reactions have been studied extensively over the past two decades. One of the early goals was to explain the barrier distributions that have been extracted from measurements [1]. Another interesting and somewhat related question is what is the influence of transfer. This issue was first raised by Beckerman et al. [2] who observed a large enhancement in the subbarrier fusion of $^{58}\text{Ni}+^{64}\text{Ni}$ compared to an interpolation between the fusion cross sections for the two symmetric systems, $^{58}\text{Ni}+^{58}\text{Ni}$ and $^{64}\text{Ni}+^{64}\text{Ni}$. A similar observation was made in the fusion of $^{40}\text{Ca}+^{48}\text{Ca}$ [3] which is strongly enhanced at subbarrier energies and suppressed at high energies compared to the expectation based on the fusion data for the two symmetric systems, $^{48}\text{Ca}+^{48}\text{Ca}$ [4] and $^{40}\text{Ca}+^{40}\text{Ca}$ [5].

It was realized early on that the influence of transfer on fusion can be large when the effective Q value for transfer is large and positive [6], as is the case for $^{58}\text{Ni}+^{64}\text{Ni}$ and $^{40}\text{Ca}+^{48}\text{Ca}$. Couplings to transfer channels with large negative Q values, on the other hand, are expected to have a much smaller effect. The coupling to such reaction channels results in an energy shift of the calculated cross section, due to an adiabatic renormalization of the ion-ion potential [7]. However, it can be difficult to disentangle this effect from uncertainties in the ion-ion potential and the effect is therefore often ignored.

A more recent observation is that fusion data are often hindered at extreme sub barrier energies [8] when compared to coupled-channels calculations that use the standard or empirical Woods-Saxon potential which has been extracted from elastic scattering data [9]. Another observation is that the data are often suppressed at energies far above the Coulomb barrier when compared to calculations that use the same potential [10]. Both phenomena and ways to explain them were discussed in a recent review of heavy-ion fusion reactions [11].

Excellent examples on all of the above phenomena are observed in the data for the fusion of ^{40}Ca with $^{90,96}\text{Zr}$ [12] and ^{48}Ca with $^{90,96}\text{Zr}$ [13]. The fusion data for $^{40}\text{Ca}+^{96}\text{Zr}$ [12] were recently supplemented with new measurements [14] that went down to a lowest cross section of $2.4 \pm 1.7 \mu\text{b}$. The data for this system are particularly interesting because they are strongly enhanced at subbarrier energies compared with the data of the other Ca+Zr systems. Moreover, they do not show any sign of a fusion hindrance at the lowest energies. These features are ascribed to the influence of couplings to transfer channels which

is expected to be strong because the effective Q values for one- and two-nucleon transfer are all positive. The influence of transfer on the fusion of $^{48}\text{Ca}+^{96}\text{Zr}$, on the other hand, is expected to be small because all of the effective Q values for transfer are large and negative.

In view of the complexity of the Ca+Zr fusion data, it is of great interest to perform a systematic coupled-channels calculations analysis of the fusion data for the four systems. The basic calculations presented here include couplings to one- and two-phonon excitations as well as mutual excitations of the low-lying surface modes in the reacting nuclei. More complex calculations that include couplings of up to three-phonon excitations and to one- and two-nucleon transfer channels are also performed. The motivation is to explore their influence on fusion and try to isolate the influence of transfer from other reaction channels.

The simplest case of the four Ca+Zr systems mentioned above is possibly the fusion of $^{48}\text{Ca}+^{96}\text{Zr}$, primarily because the effective Q values for one- and two-nucleon transfer are all negative, and the influence of transfer is therefore expected to be weak. The fusion data for this system have already been explained fairly well by coupled-channels calculations [15] that used the M3Y+repulsion (M3Y+rep) potential and included couplings to one- and two-phonon excitations of the low-lying surface modes. The potential was calculated using the double-folding technique [16] which is also used in this work.

The nuclear densities of the two calcium isotopes that are used were determined previously in Refs. [5, 17] by analyzing the fusion data for $^{40}\text{Ca}+^{40}\text{Ca}$ [5] and $^{48}\text{Ca}+^{48}\text{Ca}$ [17]. The nuclear density parameters of the two Zr isotopes are determined by analyzing the data for the ^{48}Ca induced fusion reactions with ^{90}Zr and ^{96}Zr that were measured by Stefanini et al. [13]. Having determined these parameters, one can then predict the ion-ion potentials and the cross sections for the fusion of ^{40}Ca with ^{90}Zr and ^{96}Zr . The quality of the predictions is tested by comparing to the data of Timmers et al. [12] and Stefanini et al. [14].

The basic ingredients of the coupled-channels technique are summarized in Section II. The analysis of the data for the ^{48}Ca induced fusion with ^{90}Zr and ^{96}Zr is presented in Section III. The predicted cross sections for the fusion of ^{40}Ca with the two zirconium isotopes are compared to the data in Section IV, and Section V contains the conclusions.

II. COUPLED-CHANNELS CALCULATIONS

The coupled-channels calculations that are presented are similar to those that were performed, for example, in the analysis of the fusion data for the calcium isotopes [5, 17] and for $^{48}\text{Ca}+^{96}\text{Zr}$ [15]. The main ingredients that are relevant to the discussion here are summarized below. The radii of the reacting nuclei are expressed as $R_i = R_i^{(0)} + \delta R_i$, where

$$\delta R_i = R_i^{(0)} \sum_{n\lambda\mu} \alpha_{in\lambda\mu} Y_{\lambda\mu}^*(\hat{r}), \quad (1)$$

is the nuclear surface distortion, $\alpha_{in\lambda\mu}$ are the dynamic deformation amplitudes, and \hat{r} is a unit vector along the line between the centers of the reacting nuclei.

In this work the iso-centrifugal approximation [18] is adopted in order to reduce the number of coupled equations. This approximation is equivalent to the rotating frame approximation [19, 20] in which the z -axis points along the direction of \hat{r} . The spherical harmonics that appear in Eq. (1) can therefore be replaced by $Y_{\lambda\mu}^*(\hat{r}) = \delta_{\mu,0} \sqrt{(2\lambda+1)/(4\pi)}$. That implies that the magnetic quantum numbers of the reacting nuclei are conserved. Since the magnetic quantum numbers of even-even nuclei are zero in the entrance channel, they will remain zero throughout the reaction.

The off-diagonal matrix elements of the surface distortion, Eq. (1), that connect the ground state $|0\rangle$ to an excited state $|in\lambda 0\rangle$ in nucleus i , has the following form in the rotating frame approximation (see Refs. [21, 22])

$$\langle in\lambda 0 | \delta R_i | 0 \rangle = \frac{\beta_{in\lambda} R_i^{(0)}}{\sqrt{4\pi}}. \quad (2)$$

Here λ is the multipolarity of the excitation and $\beta_{in\lambda}$ is the deformation parameter. There are actually two types of deformation parameters, one associated with the nuclear induced excitation, $\beta_{n\lambda}^N$, and one with Coulomb excitation, $\beta_{n\lambda}^C$.

The nuclear induced excitations are generated in this work by an expansion of the nuclear field up to second order in the total nuclear surface distortion, $\delta R = \delta R_1 + \delta R_2$. The nuclear interaction is therefore approximated by [21–23]

$$V_N = U(r) - \frac{dU(r)}{dr} \delta R + \frac{1}{2} \frac{d^2U(r)}{dr^2} \left((\delta R)^2 - \langle 0 | (\delta R)^2 | 0 \rangle \right), \quad (3)$$

where $U(r)$ is the ion-ion potential, which is the nuclear interaction in the entrance channel. The expression (3) has been constructed in such a way that the ground state expectation

value $\langle 0|V_N|0\rangle$ is identical to the ion-ion potential $U(r)$. The off-diagonal matrix elements of the nuclear interaction can be generated in the harmonic approximation from matrix elements of the form given in Eq. (2).

The Coulomb excitation is usually described by an expansion of the Coulomb field up to first order in the surface deformation, because it has been shown by Hagino et al. [24] that higher-order corrections to the Coulomb field can safely be ignored. The expression for the Coulomb field is therefore [21, 22],

$$V_C = \frac{Z_1 Z_2 e^2}{r} + \frac{Z_1 Z_2 e^2}{r} \sum_{in\lambda} \frac{3}{2\lambda + 1} \left(\frac{R_i^C}{r}\right)^\lambda \sum_{\mu} \alpha_{in\lambda\mu} Y_{\lambda\mu}^*(\hat{r}), \quad (4)$$

where $R_i^C = 1.20 A_i^{1/3}$ is the Coulomb radius of nucleus i . Matrix elements of the Coulomb interaction (4) are determined by matrix elements of the surface deformation [22],

$$\langle in\lambda|\alpha_{in\lambda\mu}|0\rangle = \frac{\beta_{in\lambda}^C}{\sqrt{2\lambda + 1}}, \quad (5)$$

which are here expressed in terms of the Coulomb deformation parameters $\beta_{n\lambda}^C$. These parameters can be obtained from the so-called reduced transition probability $B(E\lambda)$ that can be found, for example, in Refs. [25, 26]. The relation between the two quantities is [22]

$$B(E\lambda, 0 \rightarrow n\lambda) = \left(\frac{3Ze\beta_{n\lambda}^C R^\lambda}{4\pi}\right)^2. \quad (6)$$

The nuclear deformation parameter $\beta_{n\lambda}^N$ is often assumed to be identical to the Coulomb deformation parameter simply because other information is not available. However, the nuclear deformation parameters have in some cases been determined by analyzing the angular distributions for inelastic scattering.

Fusion data of lighter and medium heavy systems can often be explained fairly well by coupled-channels calculations that are based on the second-order nuclear (3) and the first-order Coulomb (4) interactions and include up to two-phonon excitations. This model is also the starting point of the calculations performed in this work. However, it is necessary to consider higher-order couplings and include higher multiphonon excitations if one wants to explain the fusion data of heavy and soft systems (see Refs. [23, 24].) The influence of up to three-phonon excitations will therefore be explored but the expansion of the nuclear interaction, Eq. (3), will still be truncated at the second-order level.

The fusion cross section is primarily determined by the ingoing flux obtained from the ingoing-wave boundary conditions that are imposed at the minimum of the pocket in the

entrance channel potential. This definition is supplemented with the absorption in a weak and short-ranged imaginary potential,

$$W(r) = \frac{-W_0}{1 + \exp((r - R_w)/a_w)}, \quad (7)$$

where R_w is the position of the pocket in the entrance channel potential. The diffuseness a_w is set to 0.2 fm, whereas the strength W_0 is set to either 2 MeV or 5 MeV as explained in the description of the calculations. The strength of the short-ranged imaginary potential is not a serious issue when a standard Woods-Saxon potential is used because the calculated cross sections are relatively insensitive to the value of W_0 . It is a more delicate issue when the shallow M3Y+rep potential is used.

A. The ion-ion potential

The coupled-channels calculations are based on the M3Y+repulsion (M3Y+rep) potential, the calculation of which is described in Ref. [16]. The M3Y potential alone, U_{M3Y} , is calculated using the double-folding expression,

$$U_{\text{M3Y}}(\mathbf{r}) = \int d\mathbf{r}_1 \int d\mathbf{r}_2 \rho_1(\mathbf{r}_1) \rho_2(\mathbf{r}_2) v_{\text{M3Y}}(\mathbf{r} + \mathbf{r}_2 - \mathbf{r}_1), \quad (8)$$

where $\rho_i(r)$ are the nuclear densities of the reacting nuclei, and $v_{\text{M3Y}}(r)$ is the effective M3Y (direct + exchange) interaction. The densities are parametrized in terms of the symmetrized fermi function introduced in Ref. [27] with a fixed diffuseness and an adjustable radius.

The M3Y potential U_{M3Y} is extremely deep for overlapping nuclei and it produces a pocket in the entrance channel potential that is deeper than the ground state energy of the compound nucleus. This unphysical condition is repaired by introducing a repulsive potential. The repulsive part U_{rep} of the M3Y+rep potential [16], $U_{\text{M3Y}} + U_{\text{rep}}$, is calculated from an expression that is similar to Eq. (8),

$$U_{\text{rep}}(\mathbf{r}) = \int d\mathbf{r}_1 \int d\mathbf{r}_2 \hat{\rho}_1(\mathbf{r}_1) \hat{\rho}_2(\mathbf{r}_2) v_{\text{rep}}(\mathbf{r} + \mathbf{r}_2 - \mathbf{r}_1). \quad (9)$$

Here the effective interaction v_{rep} is assumed to be a simple contact interaction,

$$v_{\text{rep}}(\mathbf{r}) = V_{\text{rep}}\delta(\mathbf{r}). \quad (10)$$

The nuclear densities $\hat{\rho}_i(r)$ that are used to calculate the repulsive potential, Eq. (9), are assumed to have the same radii as those that are used to calculate the M3Y potential, U_{M3Y} , but the diffuseness a_r is different and is treated as an adjustable parameter [16].

The strength of the repulsive interaction V_{rep} is calibrated (once the radii and value of a_r has been chosen) to produce a nuclear incompressibility K of the compound nucleus that is consistent with the values tabulated in the work of Myers and Świątecki [28]. The procedure is explained in detail in Ref. [16]. There are therefore two adjustable parameters for each of the reacting nuclei, namely, the radius of the density and the diffuseness associated with the repulsive part of the interaction. While the height of the Coulomb barrier is primarily determined by the radius parameter, the diffuseness parameter a_r controls the thickness of the barrier and the depth of the pocket in the entrance channel potential. Both parameters are adjusted to optimize the fit to the fusion data. This scheme was used in the analysis of the fusion data for the two symmetric systems, $^{40}\text{Ca}+^{40}\text{Ca}$ [5] and $^{48}\text{Ca}+^{48}\text{Ca}$ [17], and the parameters of the densities that were obtained are shown in Table II.

By adopting the density of ^{48}Ca that was obtained in a previous work [17] one can now analyze the $^{48}\text{Ca}+^{90,96}\text{Zr}$ fusion data and determine the density parameters of the two zirconium nuclei. Actually, since the point-proton densities are fairly well known from electron scattering experiments, it is better to adopt these densities and instead calibrate the point-neutron densities to provide an optimum fit to the fusion data. The parameters that have been obtained are shown in Table II. The results suggest that both isotopes have a neutron skin, which is defined as the difference between the RMS radii if the point-neutron and point-proton densities,

$$\delta r_{np} = \langle r^2 \rangle_n^{1/2} - \langle r^2 \rangle_p^{1/2}. \quad (11)$$

As a consistency check of the analysis, one can compare the neutron skin thickness extracted from the fusion data to the values that have been obtained in other experiments. Thus, if the extracted neutron skin is too thick, that would indicate that some of the couplings were too weak or that some important reaction channels were missing in the coupled-channels calculations. On the other hand, if the extracted neutron skin is too thin, that would indicate that the coupling strengths to certain reaction channels were too strong.

We have chosen in this work to compare the extracted neutron skin thickness to the values that have been obtained in anti-proton experiments [29]. One reason is that systematic results have been obtained with this method for a wide range of nuclei. Another reason is that the uncertainties of this method are not unreasonable in comparison to other methods. A better value could possibly be obtained by measuring the parity-violating asymmetry in the elastic scattering of polarized electrons but that has not yet been achieved [30].

The values of the neutron skin thickness obtained with different methods are compared in Fig. 7 of Ref. [31] for a ^{208}Pb target. The figure shows that the anti-proton experiment [29] ($\delta_{np} = 0.15 \pm 0.02$ fm) is consistent with a measurement of the dipole polarizability obtained in inelastic proton scattering [31] ($\delta r_{np} = 0.165 \pm 0.026$ fm). The elastic proton scattering data give slightly larger values of the neutron skin thickness but a previous analysis at 800 MeV [32] gave a result ($\delta r_{np} = 0.14 \pm 0.04$ fm) that is close to the value of the anti-proton experiment. Thus it appears that proton and anti-proton experiments are in fairly good agreement for ^{208}Pb , and a similar result ($\delta_{np} = 0.16 \pm 0.04$ fm) has also been obtained in ($^3\text{He}, t$) charge-exchange reactions [33]. The parity-violating asymmetry experiment [30], on the other hand, gave a larger and more uncertain value, $\delta r_{np} = 0.33_{-0.18}^{+0.16}$ fm.

B. Nuclear structure input

The deformation parameter for Coulomb and nuclear induced excitations, β_λ^C and β_λ^N , respectively, are not always identical as discussed in Sec. II. An example is the excitation of the calcium isotopes [35], where an analysis of the $^{16}\text{O}+^{40,48}\text{Ca}$ elastic and inelastic scattering data gave nuclear deformation parameters that were significantly smaller than the adopted values for Coulomb excitation. The two types of deformation parameters are compared in Table I in terms of the quantity

$$\sigma_\lambda = \frac{\beta_\lambda R}{\sqrt{4\pi}}, \quad (12)$$

which is just the matrix elements of the surface distortion, Eq. (2). The nuclear deformation parameters for the two zirconium isotopes are not known so they are assumed to be identical to the Coulomb deformation parameters.

The basic structure input to the calculations is summarized in Table I. When excitations of multiphonon states are considered, it is assumed that the couplings to these states can be calculated in the harmonic oscillator model from the values of β_λ that describe the one-phonon excitation. It must be emphasized that this approximation may not always be realistic and the calculations that include multiphonon excitations may therefore be uncertain.

The basic two-phonon calculation includes one- and two-phonon excitations of the low-lying 2^+ and 3^- states in projectile and target, as well as mutual excitations of these states. That results in a total of 15 channels (including the elastic) and is referred to as the Ch-15

calculation. The 5^- state in ^{48}Ca is relatively weak and is ignored. The 5^- excitation in ^{90}Zr is stronger but it is combined with the 3^- excitation in the same nucleus into one effective 3^- channel. The basic two-phonon calculation performed for the ^{48}Ca induced fusion with ^{90}Zr and ^{96}Zr are therefore Ch-15 calculations and they are reported in Section III.

The 5^- excitation in ^{40}Ca is relatively strong and it is therefore included explicitly in the calculations of the ^{40}Ca induced fusion reactions with the zirconium isotopes. On the other hand, the two-phonon excitations of the 2^+ states in projectile and target are relatively weak and they are therefore ignored, and so is the two-phonon excitation of the 5^- state. The basic two-phonon calculation (that includes mutual excitations) has 18 coupled channels, and the results of this Ch-18 calculation are reported in section IV.

The sensitivity to multiphonon excitations is investigated by considering the effect of up to three-phonon excitations. These calculations are not meant to be complete because the number of channels can easily become very large. The detailed calculations are described in Sections III and IV.

C. Transfer reactions

The effective Q value for transfer reactions is defined in terms of the true Q value [6],

$$Q_{eff} = Q + \Delta V_{CB}, \quad (13)$$

where ΔV_{CB} is difference in the height of the Coulomb barrier in the entrance and in the exit channel. The general experience is that couplings to transfer reactions with positive effective Q values can have a strong effect and enhance the subbarrier fusion cross section [6], whereas the effect of transfer channels with large negative Q values is weaker and leads to an adiabatic renormalization of the ion-ion potential [7].

The effective Q values for the most favorable one- and two-nucleon transfer reactions in $\text{Ca}+\text{Zr}$ collisions are shown in Table III. They are all negative for $^{48}\text{Ca}+^{96}\text{Zr}$ and couplings to transfer channels were ignored in the previous work [15] but they will be considered in this work. The effective Q values for some of the other isotope combinations are positive and their influence on fusion will therefore be considered. The effective Q values for pair-transfer are particularly large and positive in $^{40}\text{Ca}+^{96}\text{Zr}$ collisions and the influence of pair-transfer is expected to play an important role in the fusion of this system.

The influence of transfer reactions is described by the model introduced in Ref. [36]. The model assumes that excitations and transfer are independent degrees of freedom. The two-nucleon transfer is treated both as a direct and a successive process. The direct two-nucleon (or pair) transfer is described by the monopole form factor [37],

$$F_{2p} = -\sigma_{2p} \frac{dU}{dr}. \quad (14)$$

The parameters of the one-nucleon transfer channels are specified later on for each of the four systems. It is unfortunately not feasible to consider all transfer channels. The choice of the transfer mode considered, either proton or neutron, is therefore made according to which transfer mode has the larger Q value for pair-transfer. The strength of the pair-transfer, σ_{2p} , is adjusted in each case to optimize the fit of the calculated cross section to the fusion data. This empirical approach is adopted here because the pair transfer strength is not always known. The approach could be misleading because the adjusted strength could very well simulate the effect of couplings to other reaction channels that are not included explicitly in the calculation. On the other hand, if the cross sections for one- and two-nucleon transfer were known experimentally, one could calibrate the strengths of the transfer couplings so that the transfer data were reproduced as it was done in Ref. [36].

The influence on fusion of a particular reaction channel is primarily determined by the Q value of the reaction and by the strength of the coupling at the Coulomb barrier according to the constant coupling model of Dasso et al. [38]. The influence of the direct two-nucleon transfer is therefore expected to be stronger than the influence of one-nucleon transfer because the pair-transfer form factor, Eq. (14), is short ranged and relatively large at the Coulomb barrier, whereas the one-nucleon transfer form factor has a longer range and is relatively weak at the location of the Coulomb barrier. The cross section for one-nucleon transfer may very well be larger than the cross section for the two-nucleon transfer but that does not necessarily imply that the one-nucleon transfer has a large impact on fusion.

The couplings to one- and two-nucleon transfer are included in the coupled-channels calculations as described in the model of Ref. [36]. The model assumes as mentioned earlier that excitations and transfer are independent degrees of freedom. Thus, if there are 15 elastic and inelastic channels in the entrance channel mass partition, then the number is 30 channels (Ch-30) when one-nucleon transfer is included, and 45 channels (Ch-45) when both one-and two-nucleon transfer is considered.

III. ANALYSIS OF ^{48}Ca INDUCED FUSION

The $^{48}\text{Ca}+^{90,96}\text{Zr}$ fusion data [13] are analyzed by coupled-channels calculations that use the M3Y+rep, double-folding potential. The nuclear density of ^{48}Ca was determined previously [17] by analyzing the $^{48}\text{Ca}+^{48}\text{Ca}$ fusion data [4] and it is used here to determine the densities of the two zirconium isotopes that provide the best fit to the $^{48}\text{Ca}+^{90,96}\text{Zr}$ fusion data. The repulsive part of the M3Y+rep interaction is calibrated to produce the incompressibilities $K = 227.9$ and 223.7 MeV, respectively, that are predicted for the two compound nuclei, ^{138}Nd and ^{144}Nd [28]. The overall systematic uncertainty of the experiment [13] is 14%, whereas the relative errors are mainly determined by statistics. A systematic error of 5% is therefore adopted in the χ^2 analysis of the data.

The data are also analyzed by adopting the standard Woods-Saxon parametrization of the ion-ion potential [9]. The best fit to the data is achieved by adjusting the radius of the Woods-Saxon well. Some of the results are reported here because they provide useful information when compared to the results obtained with the M3Y+rep potential. Thus a large value of the χ^2/N obtained with the Woods-Saxon potential may indicate a hindrance of the fusion data at very low energies, as discussed by Jiang et al. [8], or a suppression of the fusion data at high energies, as discussed by Newton et al. [10]. The χ^2/N is expected to be smaller when the M3Y+rep potential is used because this potential usually resolves the discrepancies with the data both at very low and very high energies [16]. However, the situation is not always so straightforward because there are other issues that can play a role, for example, the influence of couplings to multiphonon excitations and transfer reactions.

The results of the analysis of the fusion data that is based on the M3Y+rep potential and includes couplings to one- and two-phonon excitations are shown in Fig. 1. The calculations have 15 channels and are denoted Ch-15 in the figure. The neutron densities of the two zirconium isotopes were adjusted as described previously to optimize the fit to the data. The two parameters of the neutron density that were obtained, namely, the radius R_n and the diffuseness a_r associated with the repulsion, are shown in Table IV and V. Also shown is the height V_{CB} of the Coulomb barrier in the entrance channel, as well as the quality of fit to the data in terms of the χ^2/N . The fits to the data in Ch-15 calculations are not perfect and it is discussed below how they can be improved by considering the effect of transfer and multiphonon excitations.

A. $^{48}\text{Ca}+^{90}\text{Zr}$

The fit to the $^{48}\text{Ca}+^{90}\text{Zr}$ fusion data shown in Fig. 1 is poor. It is seen that the Ch-15 calculation underpredicts the data at subbarrier energies (see Fig. 1A) and exceeds them at high energies (see Fig. 1B). It turns out that a previous analysis that used a standard Woods-Saxon potential with diffuseness $a = 0.68$ fm gave essentially the same result [13]. It is shown below that it is possible to achieve a much better fit by including couplings to one- and two-proton transfer reactions. The calculation is denoted Ch-45 and contains 45 coupled channels as explained in section II.C.

Effects of transfer. The best fit to the data in Ch-45 calculations is achieved by adjusting the strength σ_{2p} of the two-proton transfer, Eq. (14), as well as the radius of the neutron density in ^{90}Zr . The effective Q value for the one-proton transfer, from fully occupied $p_{1/2}$ orbit in ^{90}Zr to the unoccupied $f_{7/2}$ proton orbit outside ^{48}Ca , is set to -0.92 MeV, (see Table III.) The effective Q value for two-proton transfer is +2.22 MeV but the value $Q_{2p}=+1$ MeV is adopted here because it provides the best fit to the data. The neutron transfer is ignored because the Q values are negative so the influence on fusion is expected to be smaller.

The adjusted Ch-45 calculations are in good agreement with the data, with a $\chi^2/N = 1.06$ for the standard Woods-Saxon potential, and $\chi^2/N = 0.69$ for the M3Y+rep potential (see Table IV.) The two calculations are compared to the data in Fig. 2. The calculation with the Woods-Saxon potential (WS Ch-45) exceeds the high energy data. This is in qualitative agreement with the systematics found by Newton et al. [10]. The calculation based on the M3Y+rep potential resolves the discrepancy at high energies and provides an almost perfect fit. The adjusted pair-transfer strength is $\sigma_{2p} = 0.15$ fm in both calculations and it produces a pair-transfer cross section of the order of 80 mb at 110 MeV.

The influence of transfer on the fusion of $^{48}\text{Ca}+^{90}\text{Zr}$ is relatively modest at high energies, where it reduces the cross section slightly and brings it into better agreement with the data. The effect is much larger at low energies. This can be seen in Fig. 3, where the results of Ch-15 and Ch-45 calculations are compared to the data. Both calculations apply the M3Y+rep potential that gives the best fit in Ch-45 calculations (see Table IV). The fit of the Ch-15 calculation is therefore not as good as obtained in the Ch-15 calculation shown in Fig. 1. It is shown here so one can see directly the effect of transfer by comparing the Ch-15 and Ch-45 calculations.

Effects of multiphonon excitations. In order to limit the number of channels in calculations that include up to three-phonon excitations, we first exclude the two-phonon excitations of the 2^+ states in projectile and target because the excitation strength is relatively weak (see Table I, where $\beta_2 \approx 0.1$). The number of channels in the basic two-phonon calculation is therefore reduced from 15 to 13 channels. This calculation is supplemented with the simultaneous excitation of 3 different one-phonon states and with the combined excitation of a one-phonon and a two-phonon state. The explicit three-phonon excitation of any particular one-phonon state is ignored. The total number of channels in the ^{48}Ca induced reactions is therefore 23 and the calculation is referred to as the Ch-23 three-phonon calculation.

The effect of couplings to three-phonon excitations turns out to be relatively modest. The best Ch-23 calculation has a χ^2/N of 2.3 in contrast to the much smaller value of 0.69 obtained in the Ch-45 calculation discussed above that included the effect of transfer and two-phonon excitations. This conclusion is confirmed by Ch-69 calculations that include the combined effect of transfer and up to three-phonon excitations because the χ^2/N is the same as obtained in Ch-45 calculations (see Table IV.)

Although the couplings to three-phonon excitations do not play any major role in the overall χ^2 fit to the fusion data, their influence can be seen in the barrier distribution for fusion, which is defined as the second derivative of the energy-weighted cross section [39],

$$B(E) = \frac{d^2(E\sigma)}{dE^2}. \quad (15)$$

The distribution is calculated using the finite difference method with an energy step of $\Delta E = 2$ MeV. The distributions one obtains for the fusion of $^{48}\text{Ca}+^{90}\text{Zr}$ are illustrated in Fig. 4A. The Ch-15 calculation is seen to consist of two isolated peaks, whereas the measured distribution is broad and asymmetric. The Ch-23 calculation shows a slight improvement and so does the Ch-69 calculation but the distribution is still dominated by two peaks.

The discrepancy with the measured barrier distribution suggests that some important reaction mechanism is still missing, or maybe the reaction model used here, which assumes that excitation and transfer are independent degrees of freedom, is unrealistic. Another possibility is that couplings to a large number of (non-collective) excitation and transfer channels, with a wide range of Q values, would smear the calculated barrier distribution and bring it into better agreement with the measurement. A similar hypothesis was proposed by Yusa et al. [40] but it did not explain the data in the case they studied.

The first derivative of the energy weighted cross section is shown in Fig. 4B. By comparing the Ch-15 and Ch-23 calculations it is seen that the influence of multiphonon excitations is weak, and by comparing the Ch-23 and Ch-69 it is seen that the influence of transfer is relatively modest at high energies.

As a final test of the convergence of the results obtained in the analysis of the fusion data, it is useful to take a look at the neutron densities that have been extracted. The parameters of the assumed point-proton and the extracted point-neutron densities of ^{90}Zr are listed in Table II. From the associated RMS radii given in column 5 one can now determine the thickness of the neutron skin, δr_{np} , defined in Eq. (11). The skin thickness decreases as the number of channels increases, from $\delta r_{np} = 0.14$ fm in the Ch-15 calculation, to $\delta r_{np} = 0.08$ fm in the Ch-45 calculation. The latter value is in surprisingly good agreement with the anti-proton experiment [29] that gave the value $\delta r_{np} = 0.09 \pm 0.025$ fm.

B. $^{48}\text{Ca}+^{96}\text{Zr}$

The Ch-15 fit to the $^{48}\text{Ca}+^{96}\text{Zr}$ data shown in Fig. 1 looks reasonable and has a $\chi^2/N = 1.5$. The calculation is essentially the same that was published in Ref. [15]. There are some discrepancies at high energies (see the linear plot in Fig. 1B), where the data exceed the calculation. This is the opposite of the systematics trend discussed by Newton et al. [10]. Ways to eliminate the discrepancies are discussed below.

It is interesting that the χ^2/N shown in Table V are the same in the Ch-15 calculations that are based on the Woods-Saxon and on the M3Y+rep potential, respectively. This is misleading because the data are actually hindered at low energies compared to calculations that use a standard Woods-Saxon potential. This was already demonstrated in Ref. [15]. One would therefore expect that the M3Y+rep potential would provide the best description to the data. The main reason this is not the case is that the Ch-15 calculation, which uses the M3Y+rep potential and a weak, short-ranged imaginary potential, underestimates the data at high energies. This problem was solved in Ref. [15] by applying a stronger short-ranged imaginary potential, which should simulate the effect of couplings to channels that were not included explicitly in the calculations. It would be more satisfactory if one could explain the fusion data without resorting to a strong imaginary potential. The influence of couplings to multiphonon excitations and transfer reactions is therefore investigated below.

Effects of multiphonon excitations. The influence of multiphonon excitations can be seen in the barrier distribution for fusion. This was demonstrated in the original analysis [13], where it was shown that some of the structures that appear in the measured distribution can be explained by considering multiphonon excitations of the low-lying 3^- state in ^{96}Zr . This explanation was confirmed in Ref. [15].

The cleanest way to study the influence of multiphonon excitations is to repeat the data analysis with an increasing number of channels and plot the χ^2/N as a function of the radius R_n of the neutron density. The results of the analysis are shown in Fig. 5. The calculations employed the fixed value $W_0 = 5$ MeV of the short-ranged imaginary potential, and a fixed diffuseness of $a_r = 0.395$ fm associated with the repulsive part of the M3Y+rep potential. The latter value gives the optimum fit to the data in the Ch-15 calculations discussed above.

The χ^2/N obtained in Ch-15 and Ch-23 calculations are shown in Fig. 5. They are similar in magnitude and both have a minimum near $R_n = 5.20$ fm. It is therefore concluded that the three-phonon excitations that are included in Ch-23 calculations have a relatively modest influence on the fusion. The Ch-24 calculations which, in addition to the states of the Ch-23 calculation, include the three-phonon excitation of the low-lying 3^- state in ^{96}Zr , has a minimum near $R_n = 5.10$ fm. That is a significant change in radius, from the 5.20 fm to 5.10 fm. It implies that the neutron skin thickness of ^{96}Zr is reduced from 0.23 fm in the Ch-15 calculation to 0.16 fm in the Ch-72 calculation (see Table II.) The latter result is consistent with the neutron skin thickness $\delta r_{np} = 0.12 \pm 0.05$ fm that was obtained in the anti-proton experiment [29].

Influence of transfer. Finally, the influence of transfer channels is studied in Ch-72 calculations that are based on the same excitation channels that were used in the Ch-24 calculations discussed above and include, in addition, the one- and two-neutron transfer. The neutron transfer channels are chosen here because they have the most favorable Q values (see Table III.) The one-neutron transfer, from the fully occupied $d_{5/2}$ orbit in ^{96}Zr to the unoccupied $p_{1/2}$ state in ^{48}Ca , has the effective Q value $Q_{1n} = -2.64$ MeV and the two-neutron transfer has the Q value $Q_{2n} = -2.67$ MeV. The best fit to the data in Ch-72 calculations is achieved for a modest pair-transfer strength of $\sigma_{2p} = 0.05$ fm.

The χ^2/N for Ch-72 calculations is shown in Fig. 5. It has a minimum at the radius $R_n = 5.10$ fm which gave the best fit in the Ch-24 calculations discussed above and is consistent with the measured neutron skin thickness of Ref. [29]. In other words, the

influence of transfer does not affect the radius of the neutron density that is extracted from the analysis of the fusion data. However, it improves the fit to the data by reducing the χ^2/N considerably.

The calculated cross sections, obtained with the radius $R_n = 5.1$ fm of the neutron density in ^{96}Zr , are compared to the data in Figs. 6A. It is seen that it is the combined effect of couplings to multiphonon excitations (in Ch-24 calculations) and one- and two-neutron transfer reactions (in Ch-72 calculations) that provides the good agreement with the data at low energies. At high energies, it is primarily the effect of the multiphonon excitations in Ch-24 calculations that brings the calculated cross section into good agreement with the data. This is illustrated in Fig. 6B but it is difficult to see because the Ch-24 calculation is covered by the Ch-72 calculation that in addition includes the effects of transfer. In other words, the influence of transfer is small at high energies.

Derivatives of the cross section. At this point it is of interest to compare the barrier distribution, Eq. (15), extracted from the experiment to some of the calculations discussed above. The comparison is made in Fig. 7A. It is seen that the barrier distribution for the best Ch-15 calculation consists of two strong peaks and a broader bump near 105 MeV. The Ch-24 calculation has three major peaks that agree fairly well with the structures that are observed in the measured barrier distribution. Finally, the best Ch-72 calculation shows that the influence of transfer is minor but it does improve the shape of the distribution slightly in comparison to the measured barrier distribution.

A good way to illustrate the behavior of the cross sections at high energies is to plot the derivative of the energy-weighted cross sections. The measured and calculated results are shown in Fig. 7B. The calculations were all performed with the same M3Y+rep potential that provides the optimum fit to the data (as discussed above) in Ch-24 and Ch-72 calculations and is determined by the neutron density with the radius $R_n = 5.10$ fm. It is seen that the Ch-15 calculation does a poor job in reproducing the data, whereas the Ch-24 and Ch-72 calculations give almost identical results and are both in excellent agreement with the high energy data.

It should be emphasized that there are uncertainties in the choice of the nuclear structure input to multiphonon excitations. For example, the multiphonon excitations are described by the harmonic oscillator model but that may not be a realistic assumption. It is also assumed that the β_λ values are the same for the Coulomb and nuclear induced excitations of

the zirconium isotopes but that is not necessarily a valid assumption. On the other hand, the excellent agreement with the fusion data that is achieved when the three-phonon octupole excitation of ^{96}Zr is included, and the consistency of the extracted neutron density with the measured neutron skin, is very encouraging. These findings will hopefully stimulate a search for such multiphonon excitations in nuclear structure measurements.

IV. PREDICTIONS OF THE ^{40}Ca INDUCED FUSION

The nuclear density of ^{40}Ca that was determined in a previous analysis of $^{40}\text{Ca}+^{40}\text{Ca}$ fusion data [5] can now be combined with the densities of the two zirconium isotopes to calculate the M3Y+rep potentials for $^{40}\text{Ca}+^{90,96}\text{Zr}$. The repulsive part of the interaction is calibrated to produce the incompressibilities $K = 232.1$ and 229.1 MeV, respectively, that are predicted for the two compound nuclei, ^{130}Nd and ^{136}Nd [28].

The basic two-phonon calculation for the ^{40}Ca induced fusion reactions has 18 channels as described in Sect. II.B. The three-phonon calculation for the fusion of $^{40}\text{Ca}+^{96}\text{Zr}$ that is built on the Ch-18 two-phonon calculation has 36 channels. That number is reduced to 30 channels by eliminating the states with an excitation energy larger 10 MeV. A similar Ch-30 calculation is constructed for $^{40}\text{Ca}+^{90}\text{Zr}$ by eliminating excitations larger than 10.5 MeV.

A. $^{40}\text{Ca}+^{90}\text{Zr}$

The cross sections one obtains for this system in the Ch-18 coupled-channels calculations are shown by the (green) dashed curve in Fig. 8. The calculation under-predicts the low-energy data as illustrated in Fig. 8A, and it is also too small at high energies as shown in Fig. 8B. One way to reduce the discrepancies with the data is to include couplings to one- and two-proton transfer channels. The effective Q value for one-proton transfer, from the $d_{3/2}$ orbit in ^{40}Ca to the empty $g_{9/2}$ orbit in ^{90}Zr , is -0.73 MeV (see Table III.). The effective Q value for two-proton transfer is $+3.05$ MeV but it is set equal to $+1$ MeV in the calculations, as it was done in the calculations for $^{48}\text{Ca}+^{90}\text{Zr}$, because that value provides the best description of the fusion data. The strength of the pair-transfer σ_{2p} is adjusted to optimize the fit to the data.

Influence of transfer. The calculation with one- and two-proton transfer that is built on the

Ch-18 calculation has 54 channels and is shown by the solid curve in Fig. 8A. The optimum strength of the pair-transfer is $\sigma_{2p} = 0.035$ fm, which produces a modest pair transfer cross section of 34 mb at 110 MeV. Although the transfer improves the fit to the data, in particular at low energies, there are still some discrepancies at high energies, where the data exceed the calculated cross sections by 10-20%.

Effects of multiphonon excitations. The result of the three-phonon calculation Ch-30 is shown by the solid curve in Fig. 8B. The calculation is in slightly better agreement with the data at high energy but the overall χ^2/N is the same as obtained in the Ch-18 calculation (see Table VI.) One could also include transfer channels in combination with the Ch-30 multiphonon excitation channels discussed above. However, the resulting Ch-90 calculation does not improve the χ^2/N by much (see Table VI.) The reason is that the couplings to transfer channels enhance the fusion cross section at low energy but it does not have much effect at high energy where the discrepancy with the data is the largest.

It is surprising that multiphonon excitations apparently do not improve the fit to the $^{40}\text{Ca}+^{90}\text{Zr}$ fusion data. This statement is based on the observation that the χ^2/N is the same in the Ch-18 and Ch-30 calculations. A possible explanation for this result is that the effect of multiphonon excitations are exaggerated in the Ch-30 calculation. Since the multiphonon excitations of ^{90}Zr were tested in Sect. III.A and found to be reasonable, one could instead question the multiphonon excitations of ^{40}Ca . The octupole excitation of ^{40}Ca , for example, is very strong but it is possible that the two-phonon excitation of this state is not as collective as described by the harmonic oscillator model. In fact, it turns out that one can achieve a much better fit to the data by excluding the two-phonon excitation of the 3^- state in ^{40}Ca . The basic two-phonon calculation will then have 17 channels (Ch-17) and the basic three-phonon calculations will now contain 27 channels (Ch-27). The calculation Ch-81 that is built on the Ch-27 calculation and includes in addition couplings to the one- and two-proton transfer channels, provides the best fit to the data with a $\chi^2/N = 1.85$. The best fit is achieved with a modest pair-transfer strength of $\sigma_{2p} = 0.035$ fm.

Derivatives of the cross section. The influence of couplings to multiphonon excitations and transfer channels on the barrier distribution and the first derivative of the energy-weighted cross sections is illustrated in Fig. 9A and 9B, respectively. It is seen that the influence of multiphonon excitations in Ch-27 calculations improves the agreement with the shape of the measured barrier distribution in comparison to the Ch-18 two-phonon calculation but

some discrepancies remain. It is also seen that the influence of transfer, which improves the overall χ^2/N considerably in Ch-81 calculations, has only a minor effect on the barrier distribution and on the first derivative of the energy-weighted cross section.

The above discussion shows that the predicted ion-ion potential for $^{40}\text{Ca}+^{90}\text{Zr}$ is reasonable and provides a good starting point for the analysis of the fusion data. Moreover, the agreement of the Ch-81 calculation with the fusion data is satisfactory in view of the uncertainties that exist in the nuclear structure input to multiphonon excitations.

It should be pointed out that the fusion data for $^{40}\text{Ca}+^{90}\text{Zr}$ do not follow the trend that is observed in the fusion of other heavy-ion systems. For example, the high-energy data are enhanced compared to calculations that use a standard Woods-Saxon potential. This is illustrated in Fig. 8B where the top curve is a Ch-30 calculation that used a standard Woods-Saxon potential with an adjusted radius. It is seen that the data exceed this calculation at high energies. This is opposite to the systematics pointed out by Newton et al. [10] who showed that most data sets are suppressed at high energies compared to calculations that use a standard Woods-Saxon potential of the form proposed in Ref. [9].

Other calculations that use a standard Woods-Saxon potential were also performed. The radius of the potential was adjusted in each case to optimize the fit to the data. It turns out that the couplings to transfer channels do not improve the fit to the data. The parameters of the best Ch-18, Ch-30 and Ch-27 calculations are shown in Table VI, and it is seen that the smallest χ^2/N is achieved in the Ch-27 calculation. The fit is essentially as good as obtained in the Ch-81 calculation that used the M3Y+rep potential. The reason is that the smallest measured cross section is about 1 mb so the expected fusion hindrance at very low energies has not yet set in.

B. $^{40}\text{Ca}+^{96}\text{Zr}$

The fusion data for this system [12, 14] were recently analyzed by coupled-channels calculations that used a standard Woods Saxon potential. The Ch-23 calculations that were performed included one-, two- and some three-phonon excitations, and the Ch-69 calculations included in addition the couplings to one- and two-neutron transfer channels. The one-neutron transfer, from the fully occupied $d_{5/2}$ orbit in ^{96}Zr to the unoccupied $f_{7/2}$ state in ^{40}Ca , has an effective Q value of +0.61 MeV (see Table III), and the effective Q value

for two-neutron transfer was set to +1 MeV with a large pair-transfer strength of $\sigma_{2p} = 0.5$ fm. The radius of the Woods-Saxon well ($R = 9.60$ fm) was chosen to optimize the fit to the data above 100 MeV (see Ref. [14] for details.)

Calculations similar to those performed in Ref. [14] are repeated here with Ch-28 and Ch-84 calculations that use the same Woods-Saxon potential. The choice of channels was made because it is consistent with the best description of the $^{40}\text{Ca}+^{90}\text{Zr}$ fusion data that was achieved in the previous section with the Ch-27 and Ch-81 calculations. The only difference is that the Ch-27 calculation is supplemented with the three-phonon excitation of the soft octupole mode in ^{96}Zr . The results of the calculations are presented in Fig. 10, together with the data of Timmers et al. [12] and the new data by Stefanini et al. [14] that extend the previous measurement down to $2.4 \mu\text{b}$. It is seen that the Ch-84 calculation shown in Fig. 10B provides an excellent fit to the data at high energies. The result is similar to the Ch-69 calculation presented in Ref. [14], and the χ^2/N of the two calculations are essentially the same (see Table VII).

It is interesting to study the sensitivity to the different couplings in the high-energy behavior of the calculated cross sections. The coupling to one-phonon excitations (Ch-6) reduces the cross section compared to the no-coupling calculation (Ch-1). The effect of multiphonon excitations in the Ch-28 calculation is to enhance the calculated cross section so it exceeds the data at high energies. Finally, the coupling to transfer channels is so strong in the Ch-84 calculation that it reduces the calculated cross section at high energy and brings it into agreement with the data. In fact, this behavior was utilized in Ref. [14] to calibrate the strength of the pair-transfer coupling.

The Ch-84 calculation shown in Fig. 10A underpredicts the data the lowest energies. Although it is possible to improve the fit to the low-energy data by increasing the strength of the pair-transfer coupling, such an increase would cause a reduction of the calculated cross section at high energies, which would deteriorate to overall agreement with the data.

The most interesting question is now how well does a Ch-84 calculation that is based on the predicted M3Y+repulsion potential agree with the data. The result is shown in Fig. 11. It is seen that the prediction of the data is poor, both at low and at high energies. The poor result at low energies (see Fig. 11A) is primarily caused by the shallow pocket of the entrance channel potential which has a minimum of 87.5 MeV, whereas the data extend down to 84.2 MeV. The Ch-84 calculation has a threshold near 88 MeV but it does extend

to energies below the minimum of the pocket. One reason is that fusion can still occur below the minimum of the pocket through the pair-transfer channel, which has a positive Q value.

The failure at high energies of the calculation that is based on the predicted M3Y+rep potential is illustrated in the linear plot of Fig. 11B. The Ch-6 calculation is far below the data but the effect of multiphonon excitations in the Ch-28 calculation is to enhance the calculated cross section. However, the Ch-28 calculation shown in Fig. 11B is 10-20 % below the data, and this discrepancy increases to 30-50 % in the Ch-84 calculation where the effect of transfer is included. It is therefore not possible to improve the agreement with data by increasing the strength of the pair-transfer. A larger transfer strength may improve the calculation at energies below the Coulomb barrier but it will reduce the calculated cross section even further below the data at high energies.

The results of the data analysis are shown in Table VII. It is seen that the calculations that use the predicted M3Y+rep potential have a χ^2/N that is much larger than obtained with a standard Woods-Saxon potential. The main reasons are that the pocket in the entrance channel potential for the M3Y+rep interaction is too shallow ($V_{min}=87.5$ MeV) and the Coulomb barrier is too high ($V_{CBV}=98.13$ MeV) compared to the entrance channel potential of the adjusted Woods-Saxon potential. These features are illustrated in Fig. 12, where the entrance channel potentials of the different nuclear interactions are compared. Another observation in this figure is that the entrance channel potential for the pure M3Y interaction is very deep, even deeper than the energy of the compound nucleus ^{136}Nd , but the barrier height is slightly larger than obtained with the Woods-Saxon potential.

The systematics of the height of the Coulomb barrier for the four Ca+Zr systems and for the two types of potentials considered in this work is illustrated in Fig. 13. It is seen that the barrier heights for the Woods-Saxon and the M3Y+rep potentials are almost identical for three of the systems but they are different for $^{40}\text{Ca}+^{96}\text{Zr}$. The M3Y+rep interaction produces a Coulomb barrier that is about 1.5 MeV higher than obtained with the Woods-Saxon potential. The height obtained with the pure M3Y interaction, on the other hand, is only 0.6 MeV larger than the value obtained with the Woods-Saxon potential. This result indicates that one would achieve a better agreement with the data by simply ignoring the repulsive part of the double-folding potential. This expectation is confirmed by detailed calculations. The last two lines of Table VII show the results one obtains for the pure M3Y interaction, i. e., for $V_{rep}=0$. It is seen that the χ^2/N is much better than obtained with the

M3Y+rep potential.

The conclusion that the fusion hindrance phenomenon does not occur in the fusion of $^{40}\text{Ca}+^{96}\text{Zr}$ is supported by the fact that the adjusted Woods-Saxon, and even the pure M3Y potential provides a better description of the data than the M3Y+rep potential does. The absence of a hindrance at very low energies appears to be consistent with the fact that the Q values for pair-transfer are large and positive for this system (see Table III). The valence nucleons can therefore flow more freely from one nucleus to the other without being hindered by Pauli blocking. If this interpretation is correct, the disappearance, - or at least a reduction, of the repulsive part of the nuclear interaction should also occur in reactions of other heavy-ion systems with large positive Q values for transfer. This mechanism will affect the isotope dependence of the height of the Coulomb barrier and lower it for systems that have large positive Q values for two-nucleon transfer reactions. In this connection it would be desirable to develop a scheme by which the repulsive part of the nuclear interaction can be calculated explicitly by considering the effect of Pauli blocking.

V. CONCLUSION

We have performed a systematic coupled-channels analysis of the fusion data for the four systems, $^{40,48}\text{Ca}+^{90,96}\text{Zr}$, using both a standard Woods-Saxon and the M3Y+repulsion, double-folding potential. While it is possible to reproduce the data for three of the systems in a consistent way by using the M3Y+repulsion potential and a realistic nuclear structure input, it is not possible to explain the $^{40}\text{Ca}+^{96}\text{Zr}$ fusion data within the same framework. The data for the latter system are better described by the pure M3Y potential or by a standard Woods-Saxon potential.

One of the goals of this work was to test how well the M3Y+rep, double-folding potential can be used to predict the ion-ion potential once the densities of the reacting nuclei are known. The nuclear densities of the two calcium nuclei were determined in previous analyses of Ca+Ca fusion data. The neutron densities of the two zirconium isotopes were determined by analyzing the fusion data induced by ^{48}Ca , whereas the proton densities were constrained by electron scattering. The neutron skin thickness of each of the two zirconium isotopes extracted from the analysis of the fusion data is consistent with the results of anti-proton experiments. This is a nice consistency check of the coupled-channels calculations.

The predicting power of the double-folding method was tested by calculating the M3Y+repulsion potential for the ^{40}Ca induced reactions with the two zirconium isotopes and analyzing the fusion data with coupled-channels calculations. This approach worked fairly well for $^{40}\text{Ca}+^{90}\text{Zr}$ but it failed for $^{40}\text{Ca}+^{96}\text{Zr}$, primarily because the predicted Coulomb barrier is too high and the pocket in the entrance channel potential is too shallow.

Although the influence of transfer plays a role in explaining the fusion data for most of the Ca+Zr systems, it is only in the case of $^{40}\text{Ca}+^{96}\text{Zr}$ that transfer is expected to have a major impact. This feature was recognized in the original work of Timmers et al. [12], where the effect of transfer was expected to be the reason for the large enhancement of the measured subbarrier fusion cross sections. The surprising new result is that the ion-ion potential predicted for this system by the M3Y+rep interaction is unrealistic. The failure of the prediction is ascribed to the influence of transfer reactions which is expected to be particularly strong because the transfer Q values are large and positive and the transfer can therefore occur without the hindrance imposed by Pauli blocking.

The repulsive part of the M3Y+repulsion potential, which explains the hindrance phenomenon observed in the fusion of many heavy-ion systems at extreme subbarrier energies, is usually calibrated to produce a realistic nuclear incompressibility for overlapping nuclei. The present work suggests that the fusion hindrance and the hindrance of transfer reactions imposed by the Pauli blocking are somehow related, because they are both absent in reactions of $^{40}\text{Ca}+^{96}\text{Zr}$. In this connection it would be very attractive if one could calculate the repulsive part of the ion-ion potential by considering the effect of Pauli blocking explicitly.

The analysis of the different data sets revealed a number of interesting problems. For example, the fusion data for $^{48}\text{Ca}+^{90}\text{Zr}$ are suppressed at high energies compared to calculations that use a standard Woods-Saxon potential, but this discrepancy was removed by applying the M3Y+rep potential. Another problem is that some of the data sets are enhanced at high energies compared to coupled-channels calculations that include couplings to one- and two-phonon excitations. The problem was resolved for $^{48}\text{Ca}+^{96}\text{Zr}$ by considering the influence of three-phonon excitations. Finally, the calculated barrier distribution for fusion consists typically of a few strong peaks, whereas the measured distribution is sometimes broad and smooth. This difference may be caused by the simplified models of excitations and transfer that are used in the calculations.

A good explanation of the $^{40}\text{Ca}+^{96}\text{Zr}$ fusion data is still missing. We have shown that it

is not possible to predict the ion-ion potential reliably for this system by the double-folding technique. It appears that an adjusted Woods-Saxon potential, or even the pure M3Y potential, provides a much more realistic description. However, none of the calculations can account for the data at the lowest energies. A clear improvement of the coupled-channels calculations would be to calibrate the transfer couplings, in particular for the two-nucleon transfer, so that the transfer data were reproduced by the calculations. This approach is currently being pursued. Another possibility is to apply a more realistic ion-ion potentials in the exit channels. This idea was proposed by Sargsyan et al. [41], who used ion-ion potentials in the exit channels for transfer reactions that are different from the entrance channel potential because of deformation effects. Both approaches are worth pursuing.

Acknowledgments. We acknowledge fruitful discussions with B. B. Back and G. Montagnoli. This work was supported by the U.S. Department of Energy, Office of Nuclear Physics, Contract No. DE-AC02-06CH11357. The research leading to these results has received funding from the European Union Seventh Framework Programme FP7/2007-2013 under Grant Agreement No. 262010-ENSAR.

-
- [1] M. Dasgupta, D. J. Hinde, N. Rowley, and A. M. Stefanini, *Annu. Rev. Nucl. Part. Sci.* **48**, 401-61 (1998).
 - [2] M. Beckerman *et al.*, *Phys. Rev. Lett.* **45**, 1472 (1980).
 - [3] C. L. Jiang *et al.*, *Phys. Rev. C* **82**, 041601(R) (2010).
 - [4] A. M. Stefanini *et al.*, *Phys. Lett. B* **679**, 95 (2009).
 - [5] G. Montagnoli *et al.*, *Phys. Rev. C* **85**, 024607 (2012).
 - [6] R. A. Broglia, C. H. Dasso, S. Landowne, and A. Winther, *Phys. Rev. C* **27**, 2433 (1983).
 - [7] K. Hagino and N. Takigawa, *Prog. Theor. Phys.* **128**, 1061 (2012).
 - [8] C. L. Jiang *et al.*, *Phys. Rev. Lett.* **89**, 052701 (2002).
 - [9] Aage Winther, *Nucl. Phys. A* **594**, 203 (1995).
 - [10] J. O. Newton *et al.*, *Phys. Rev. C* **70**, 024605 (2004).
 - [11] B. B. Back, H. Esbensen, C. L. Jiang, and K. E. Rehm, *Rev. Mod. Phys.* (in press).
 - [12] H. Timmers *et al.*, *Nucl. Phys. A* **633**, 421 (1998).
 - [13] A. M. Stefanini *et al.*, *Phys. Rev. C* **73**, 034606 (2006).

- [14] A. M. Stefanini *et al.*, Phys. Lett. B **728**, 639 (2014).
- [15] H. Esbensen and C. L. Jiang, Phys. Rev. C **79**, 064619 (2009).
- [16] Ş. Mişicu and H. Esbensen, Phys. Rev. C **75**, 034606 (2007).
- [17] H. Esbensen, C. L. Jiang, and A. M. Stefanini, Phys. Rev. C **82**, 054621 (2010).
- [18] J. Gomez-Comacho and R. C. Johnson, J. Phys. G **12**, L235, (1986).
- [19] O. Tanimura, Phys. Rev. C **35**, 1600 (1987).
- [20] H. Esbensen, S. Landowne, and C. Price, Phys. Rev. C **36**, 1216 (1987).
- [21] H. Esbensen and S. Landowne, Phys. Rev. C **35**, 2090 (1987).
- [22] H. Esbensen, Phys. Rev. C **68**, 034604 (2003).
- [23] H. Esbensen, Phys. Rev. C **72**, 054607 (2005).
- [24] K. Hagino, N. Takigawa, M. Dasgupta, D. J. Hinde, and J. R. Leigh, Phys. Rev. C **55**, 276 (1997).
- [25] ENDSF, NNDS, Brookhaven National Laboratory, www.nndc.bnl.gov/ensdf
- [26] T. Kibédi and R. H. Spear, At. Data and Nucl. Data. Tables, **80**, 35 (2002).
- [27] H. Esbensen and Ş. Mişicu, Phys. Rev. C **76**, 054609 (2007).
- [28] W. D. Myers and W. J. Świątecki, Phys. Rev. C **62**, 044610 (2000).
- [29] A. Trzcińska *et al.*, Phys. Rev. Lett. **87**, 082501 (2001).
- [30] S. Abrahamyan *et al.*, Phys. Rev. Lett. **108**, 112502 (2012).
- [31] A. Tamii, P. von Neumann-Cosel, and I. Poltoratska, Eur. Ph. J. A **50**: 28 (2014).
- [32] G. W. Hoffmann *et al.*, Phys. Rev. C **21**, 1488 (1980).
- [33] Bui Minh Loc, Dao T. Khoa, and R. G. T. Zegers, Phys. Rev. C **89**, 024317 (2014).
- [34] I. Angeli, At. Data Nucl. Data Tables **87**, 185 (2004).
- [35] H. Esbensen and F. Videbaek, Phys. Rev. C **40**, 126 (1989).
- [36] H. Esbensen, C. L. Jiang and K. E. Rehm, Phys. Rev. C **57**, 2401 (1998).
- [37] C. H. Dasso and G. Pollarolo, Phys. Lett. B **155**, 223 (1985).
- [38] C. H. Dasso, S. Landowne, and A. Winther, Nucl. Phys. A **407**, 221 (1983).
- [39] N. Rowley, G. R. Satchler, and P. H. Stelson, Phys. Lett. B **254**, 25 (1991)
- [40] S. Yusa, K. Hagino, and N. Rowley, Phys. Rev. C **85**, 054601 (2012).
- [41] V. V. Sargsyan, G. G. Adamian, N. V. Antonenko, W. Scheid, and H. Q. Zhang, Phys. Rev. C **85**, 024616 (2012).

TABLE I: Adopted structure of the excited states in ^{40}Ca [5, 35], ^{48}Ca [17, 35], and $^{90,96}\text{Zr}$ [25, 26].

Note the 3^- and 5^- excitations in ^{90}Zr are combined into one effective 3^- state.

Nucleus	λ^π	E_x (MeV)	$B(E\lambda)$ (W.u.)	β_λ^C	σ_λ^C (fm)	σ_λ^N (fm)
^{40}Ca	2^+	3.904	2.26(14)	0.119	0.138	0.125
	3^-	3.737	27(4)	0.402	0.465	0.315
	5^-	4.491	16	0.297	0.344	0.175
^{48}Ca	2^+	3.832	1.71(9)	0.102	0.126	0.190
	3^-	4.507	5.0(8)	0.203	0.250	0.190
	ignore: 5^-	5.146	0.3	0.040	0.049	0.038
^{90}Zr	2^+	2.186	5.37(20)	0.092	0.140	0.140
	5^-	2.319	8.7(4)	0.108	0.164	0.164
	Ref. [26] 3^-	2.748	28.9(15)	0.210	0.319	0.319
	effective: 3^-	2.658		0.236	0.358	0.358
^{96}Zr	2^+	1.751	4(3)	0.079	0.123	0.123
	3^-	1.897	57(4)	0.295	0.457	0.457

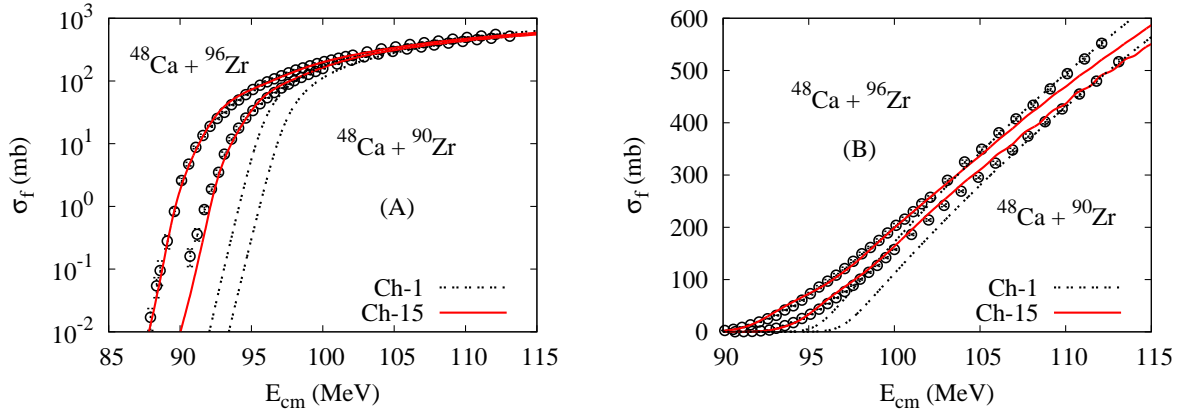


FIG. 1: (Color online) The measured cross sections for the fusion of $^{48}\text{Ca}+^{90,96}\text{Zr}$ [13] are compared to Ch-15 calculations that are based on the M3Y+rep potential. The Ch-1 no-coupling calculations are also shown. The cross sections are shown in a logarithmic (A) and a linear plot (B).

TABLE II: Parameters of the densities in $^{40,48}\text{Ca}$ and $^{90,96}\text{Zr}$: the diffuseness a_r associated with the repulsion (Eq. (7)), the radius R , the diffuseness a , and the last column is the rms radius. The matter density parameters for the calcium isotopes were determined previously [5, 17]. The second column shows the fusion reaction that was used to determine the parameters. The parameters for the proton (p) densities in ^{90}Zr and ^{96}Zr reproduce the point-proton rms radii, $\langle r^2 \rangle_{\text{pp}} = 4.198$ and 4.281 fm, respectively, extracted from the measured charge radii [34]. The parameters for the neutron (n) densities in ^{90}Zr and ^{96}Zr are from Tables IV and V.

Nucleus	Reaction	a_r (fm)	R (fm)	a (fm)	$\langle r^2 \rangle^{1/2}$ (fm)
^{40}Ca	$^{40}\text{Ca}+^{40}\text{Ca}$ [5]	0.42	3.47	0.56	3.400
^{48}Ca	$^{48}\text{Ca}+^{48}\text{Ca}$ [17]	0.43	3.798	0.54	3.562
^{90}Zr (p)			4.72	0.56	4.207
^{90}Zr (n)	$^{48}\text{Ca}+^{90}\text{Zr}$ Ch-15	0.40	4.925	0.56	4.346
^{90}Zr (n)	$^{48}\text{Ca}+^{90}\text{Zr}$ Ch-45	0.39	4.835	0.56	4.285
^{96}Zr (p)			4.86	0.55	4.284
^{96}Zr (n)	$^{48}\text{Ca}+^{96}\text{Zr}$ Ch-15	0.395	5.20	0.55	4.517
^{96}Zr (n)	$^{48}\text{Ca}+^{96}\text{Zr}$ Ch-72	0.395	5.10	0.55	4.448

TABLE III: Effective Q values (in MeV) for the most favorable one-nucleon and two-nucleon transfer reactions in $^{40}\text{Ca}+^{90,96}\text{Zr}$ and $^{48}\text{Ca}+^{90,96}\text{Zr}$ collisions, and the adopted strength σ_{2p} (in fm) of the pair transfer.

System	Q_{1n}	Q_{2n}	Q_{1p}	Q_{2p}	σ_{2p}
$^{48}\text{Ca}+^{96}\text{Zr}$	-2.64	-2.67	-4.07	-3.49	0.05
$^{48}\text{Ca}+^{90}\text{Zr}$	-2.83	-1.55	-0.92	+2.22	0.15
$^{40}\text{Ca}+^{90}\text{Zr}$	-3.50	-1.25	-0.73	+3.05	0.035
$^{40}\text{Ca}+^{96}\text{Zr}$	+0.61	+5.73	+1.55	+7.63	0.50

TABLE IV: Best fits to the $^{48}\text{Ca}+^{90}\text{Zr}$ fusion data of Ref. [13]. The χ^2/N (last column) includes a 5% systematic error. The 1st column shows the type of calculation. The 2nd column indicates the type of ion-ion potential, either the Woods-Saxon (WS) potential or the diffuseness a_r of the ^{90}Zr density associated with the repulsive part of the M3Y+rep potential. The 3rd column is the radius, either of the WS potential or the neutron density in ^{90}Zr . The radius of the proton density was set to 4.72 fm. The height of the Coulomb barrier is listed in the 4th column.

Calculation	a_r (fm)	R (fm)	V_{CB} (MeV)	χ^2/N
Ch-15	WS	9.539	96.89	3.59
Ch-45	WS	9.527	97.00	1.06
Ch-15	0.40	4.925	97.02	3.12
Ch-23	0.40	4.925	97.02	2.30
Ch-45	0.39	4.835	97.20	0.69
Ch-69	0.39	4.835	97.20	0.69

TABLE V: Best fits to the $^{48}\text{Ca}+^{96}\text{Zr}$ fusion data of Ref. [13]. The χ^2/N (last column) includes a 5% systematic error. The 1st column shows the type of calculation. The 2nd column indicates the type of ion-ion potential, either the Woods-Saxon (WS) or the diffuseness a_r of the ^{96}Zr density associated with the repulsive part of the M3Y+rep potential. The 3rd column is the radius, either of the WS potential or the neutron density in ^{96}Zr . The radius of the proton density was set to 4.86 fm. The height of the Coulomb barrier is listed in the 4th column.

Calculation	a_r (fm)	R (fm)	V_{CB} (MeV)	χ^2/N
Ch-15	WS	9.689	95.40	1.53
Ch-24	WS	9.671	95.56	3.43
Ch-15	0.395	5.20	95.54	1.49
Ch-23	0.395	5.20	95.54	2.16
Ch-24	0.395	5.10	95.86	2.22
Ch-72	0.395	5.10	95.86	0.76

TABLE VI: Analysis of the $^{40}\text{Ca}+^{90}\text{Zr}$ fusion data [13]. The χ^2/N (last column) includes a 7% systematic error. The type of calculation is listed in the 1st column. The 2nd column is the adjusted radius of the WS potential, or the radius of the neutron density in ^{90}Zr obtained in the Ch-69, M3Y+rep calculation of Table IV. The 3rd and 4th columns show the minimum of the pocket and the height of the Coulomb barrier in the entrance channel potential.

Calculation	R (fm)	V_{min} (MeV)	V_{CB} (MeV)	χ^2/N
WS Ch-18	9.312	78.91	99.49	2.60
WS Ch-30	9.302	79.08	99.58	3.92
Ws Ch-27	9.327	78.66	99.34	1.65
Ch-18	4.835	86.15	99.61	4.94
Ch-30	4.835	86.15	99.61	4.94
Ch-27	4.835	86.15	99.61	3.37
Ch-54	4.835	86.15	99.61	2.53
Ch-90	4.835	86.15	99.61	4.25
Ch-81	4.835	86.15	99.61	1.85

TABLE VII: Analysis of the $^{40}\text{Ca}+^{96}\text{Zr}$ fusion data [13]. The χ^2/N in the (last column) includes a 7 % systematic error. The type of calculation is listed in the 1st column. The 2nd column is the adjusted radius of the WS potential, or the radius of neutron density in ^{96}Zr obtained in the Ch-72, M3Y+rep calculation of Table V. The 3rd and 4th columns show the minimum of the pocket and the height of the Coulomb barrier in the entrance channel potential. The last two lines show the results of Ch-69 and Ch-84 calculations that use the pure M3Y potential, i. e., for $V_{\text{rep}}=0$.

Calculation	R (fm)	V_{min} (MeV)	V_{CB} (MeV)	χ^2/N
WS Ch-69	9.599	73.62	96.62	4.0
WS Ch-84	9.599	73.62	96.62	4.1
Ch-69	5.10	87.5	98.13	22
Ch-84	5.10	87.5	98.13	23
Ch-69 $V_{\text{rep}} = 0$	5.10	-311	97.20	5.3
Ch-84 $V_{\text{rep}} = 0$	5.10	-311	97.20	6.0

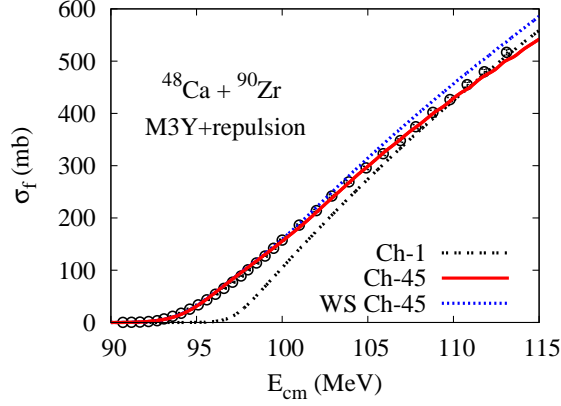


FIG. 2: (Color online) Linear plot of cross sections for the fusion of $^{48}\text{Ca}+^{90}\text{Zr}$ [13]. The best Ch-45 calculations for the Woods-Saxon (WS) and the M3Y+rep potentials are shown. The no-coupling calculation Ch-1 based on the M3Y+rep potential is also shown. All calculations use a short-ranged absorption with $W_0=2$ MeV.

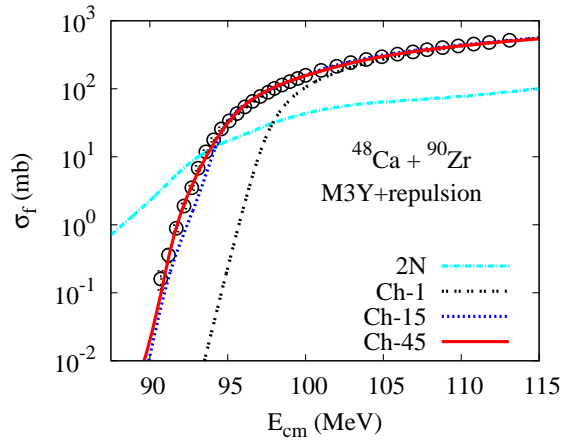


FIG. 3: (Color online) Cross sections for the fusion of $^{48}\text{Ca}+^{90}\text{Zr}$ [13] are compared to Ch-15 and Ch-45 calculations that are based on the M3Y+rep potential that gives the best fit in Ch-45 calculations. The result of the no-coupling limit (Ch-1) and the predicted 2N cross sections are also shown.

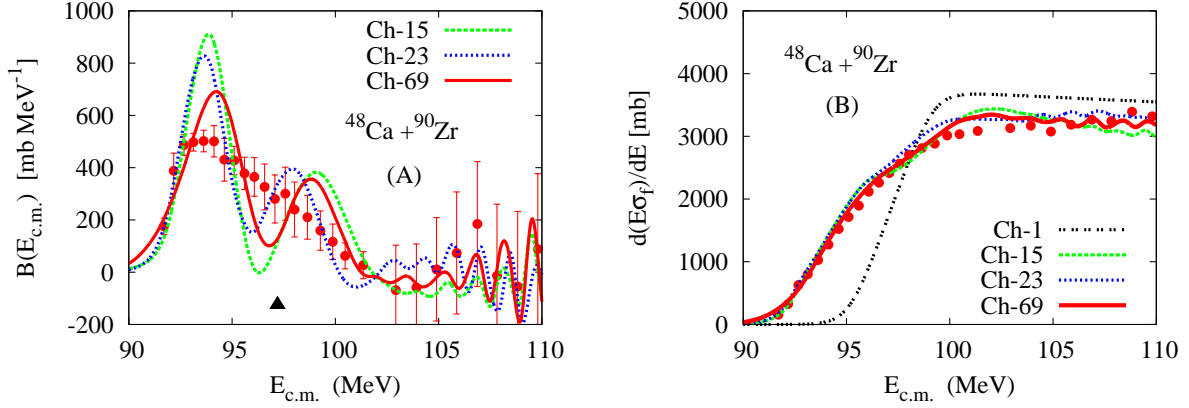


FIG. 4: (Color online) Barrier distributions (A) and the first derivative (B) of the energy-weighted cross sections for the fusion of $^{48}\text{Ca}+^{90}\text{Zr}$ [13]. The calculations used the M3Y+rep potential with the radius $R_n = 4.835$ fm of the neutron density in ^{90}Zr . The energy of the Coulomb barrier is indicated in (A) by the large triangle.

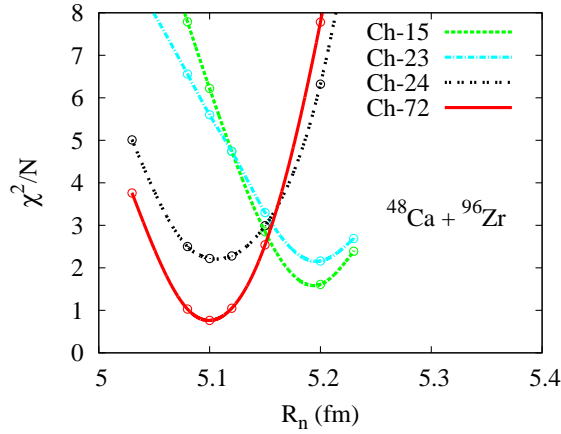


FIG. 5: (color online) The χ^2/N for the $^{48}\text{Ca}+^{96}\text{Zr}$ fusion data [13] obtained in Ch-15, Ch-23, Ch-24, and Ch-72 coupled-channels calculations as function of the radius R_n of the neutron density of ^{96}Zr .

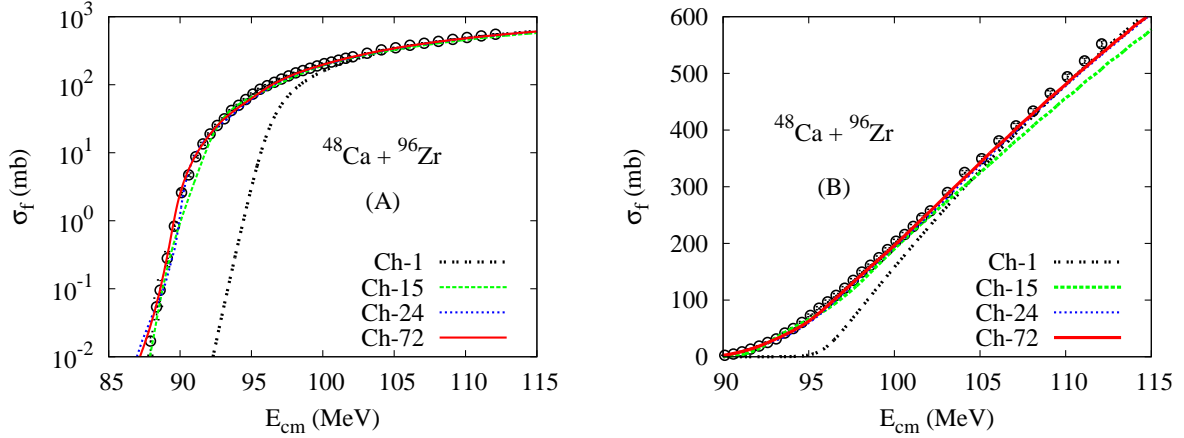


FIG. 6: (color online) Logarithmic (A) and linear plot (B) of the measured fusion cross sections for $^{48}\text{Ca}+^{96}\text{Zr}$ [13] are compared to coupled-channels calculations that are based on the M3Y+rep potential, obtained with a radius $R_n = 5.1$ fm of the neutron density in ^{96}Zr .

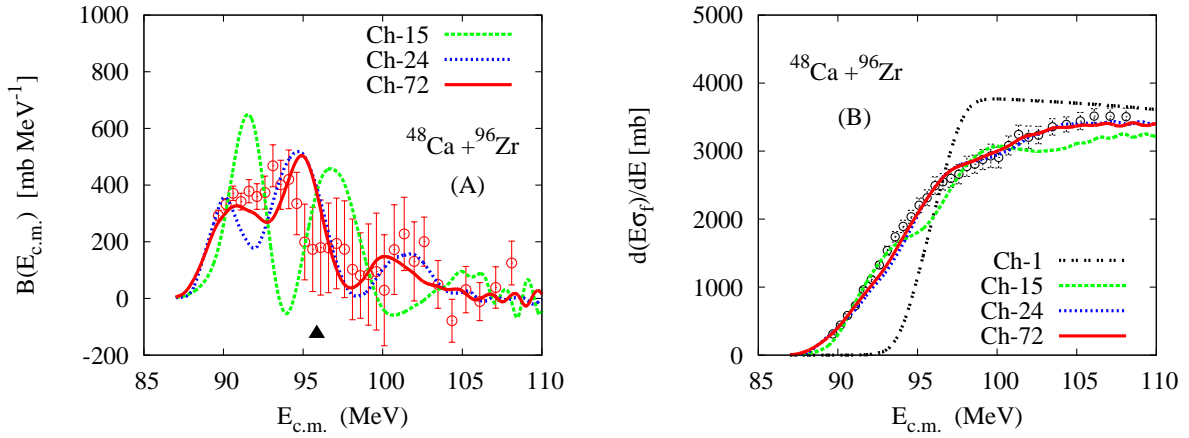


FIG. 7: (color online) Barrier distributions (A) and the first derivative (B) of the energy-weighted fusion cross sections for $^{48}\text{Ca}+^{96}\text{Zr}$ shown in Fig. 6. The M3Y+rep potential used in the calculations is based on a ^{96}Zr neutron density with radius $R_n = 5.10$ fm. The energy of the Coulomb barrier is indicated in (A) by the large triangle.

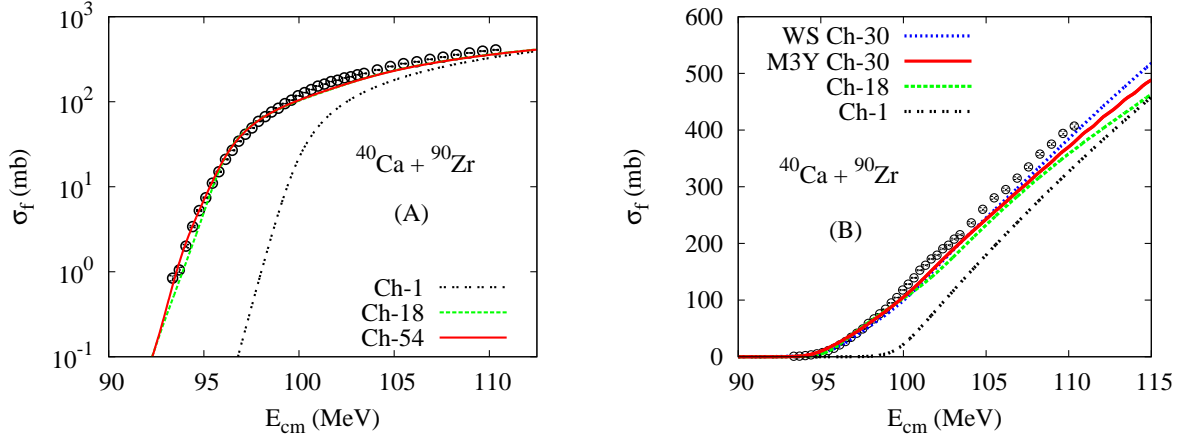


FIG. 8: (color online) Logarithmic (A) and linear plot (B) of the measured fusion cross sections for $^{40}\text{Ca}+^{90}\text{Zr}$ [12] are compared to the Ch-1, Ch-18, Ch-30 and Ch-54 calculations that are based on the predicted M3Y+rep potential. The top curve in the right panel is a Ch-30 calculation that is based on a Woods-Saxon potential.

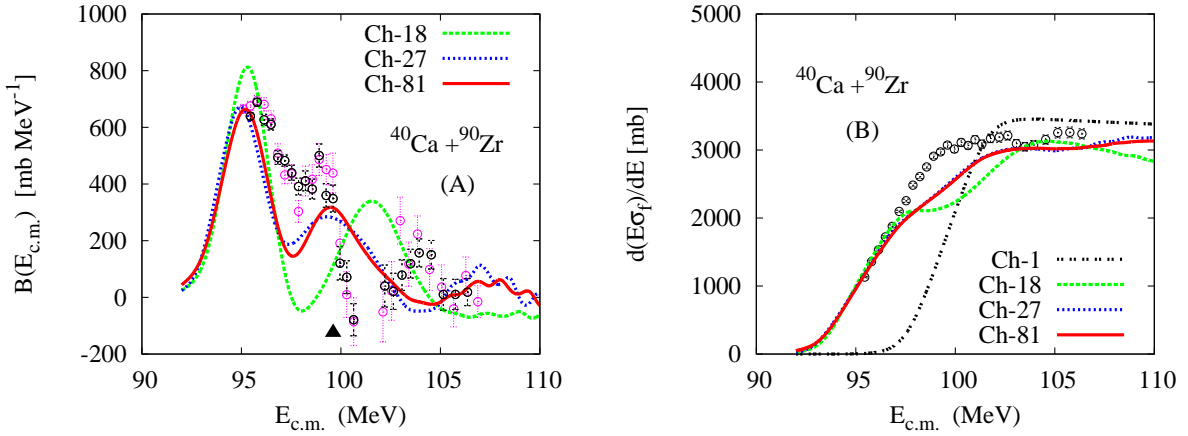


FIG. 9: Barrier distributions (A) and first derivative (B) of the energy-weighted cross sections for the fusion of $^{40}\text{Ca}+^{90}\text{Zr}$. The coupled-channels calculations use the predicted M3Y+rep potential. The large triangle in (A) indicates the energy of the Coulomb barrier.

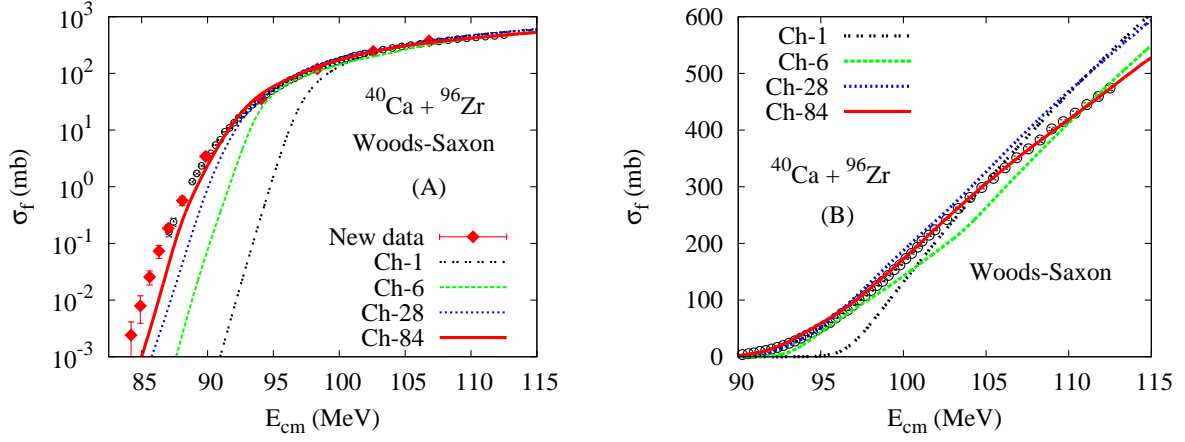


FIG. 10: (color online) Logarithmic (A) and linear plot (B) of the measured fusion cross sections for $^{40}\text{Ca} + ^{96}\text{Zr}$ (open circles [12], solid diamonds [14]). They are compared to Ch-1, Ch-6, Ch-28, and Ch-84 calculations that are based on a standard Woods-Saxon potential (see Table VII).

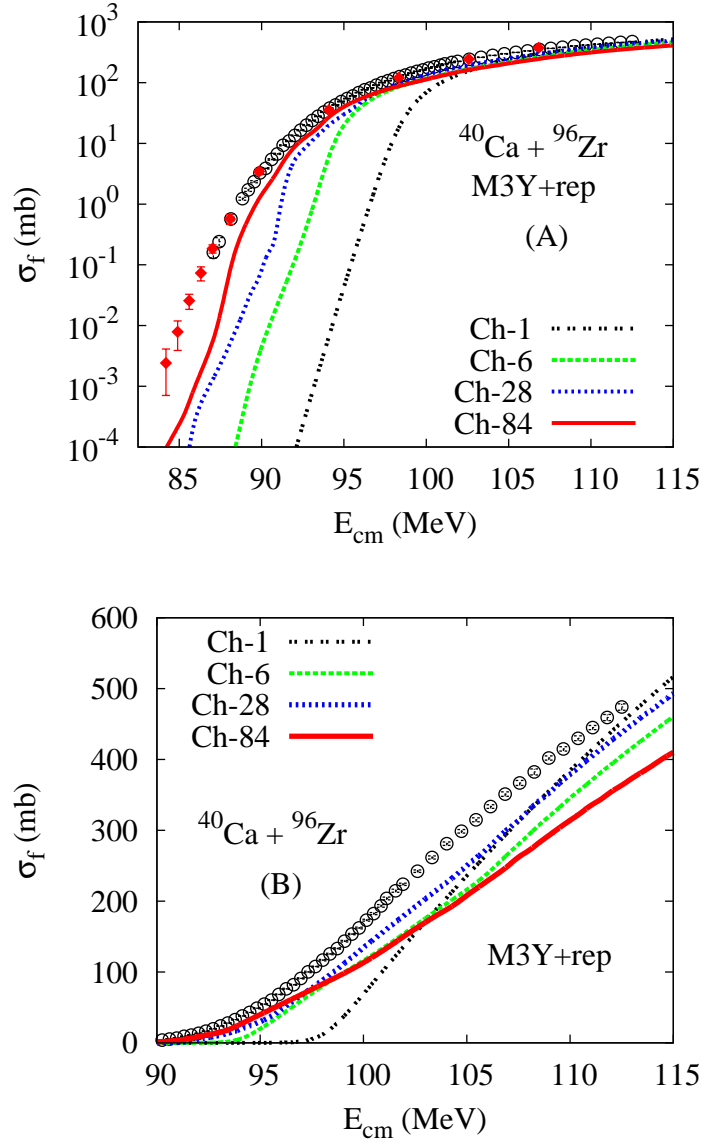


FIG. 11: (color online) Logarithmic (A) and linear plot (B) of the measured fusion cross sections for $^{40}\text{Ca} + ^{96}\text{Zr}$ (open circles [12], solid diamonds [14]). They are compared to Ch-1, Ch-6, Ch-28, and Ch-84 calculations that use the predicted M3Y+rep potential.

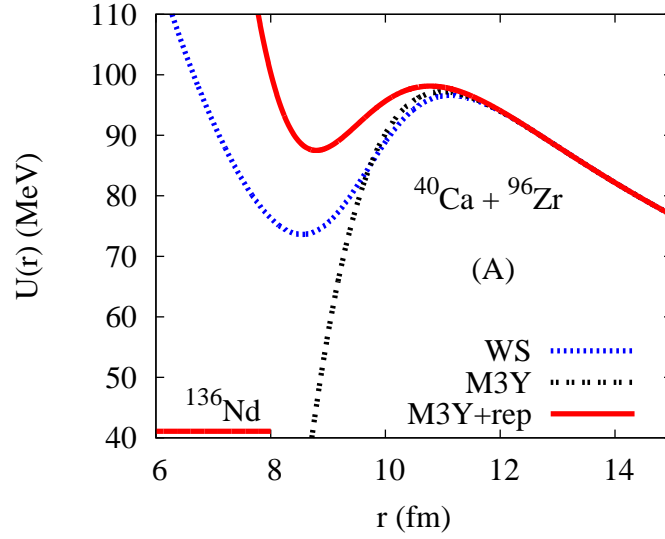


FIG. 12: (color online) Entrance channel potentials for $^{40}\text{Ca} + ^{96}\text{Zr}$ that are based on the Woods-Saxon, the M3Y+rep and the pure M3Y nuclear potentials. The energy of the compound nucleus ^{136}Nd is indicated.

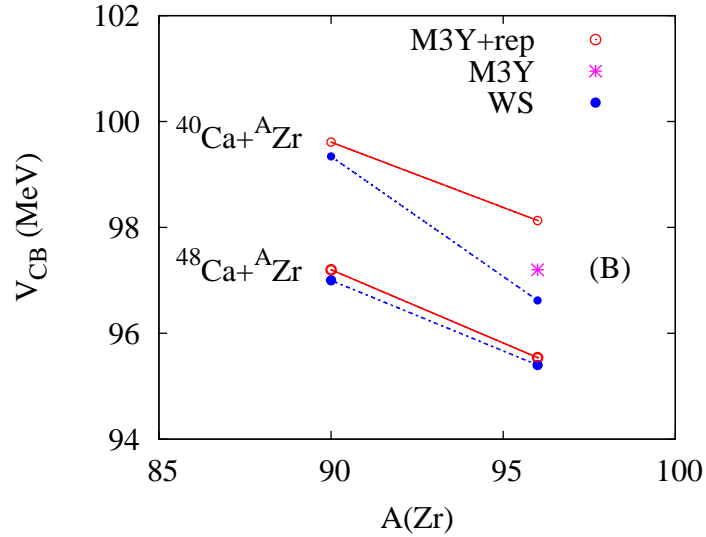


FIG. 13: (color online) Heights of the Coulomb barriers for the different Ca+Zr systems. Results are shown for the M3Y+rep and the Woods-Saxon potentials. The barrier height for the pure M3Y potential is also shown for $^{40}\text{Ca} + ^{96}\text{Zr}$.